DRAFT VERSION FEBRUARY 24, 2024
Preprint typeset using LaTeX style emulateapj v. 11/10/09

arXiv:1103.2477v2 [astro-ph.HE] 2 Oct 2011

DISCOVERY OF A SIGNIFICANT MAGNETIC CV POPULATION IN THE LIMITING WINDOW

JAESUB HONG[1*], MAUREEN VAN DEN BERG[2], JONATHAN E. GRINDLAY[1],
MATHIEU SERVILLAT[1], AND PING ZHAO[1]

Draft version February 24, 2024

ABSTRACT

We have discovered 10 periodic X-ray sources from the 1 Ms *Chandra* ACIS observation of the Limiting Window (LW), a low extinction region ($A_V \sim 3.9$) at 1.4° south of the Galactic center. The LW provides a rare opportunity of studying the Galactic Bulge sources without obscuration from molecular clouds. Using the early 100 ks *Chandra* exposure and the *HST* observation that covers five of these sources, we have reported three of them as candidate CVs or accreting binaries, based on their blue optical colors, excess Hα fluxes, and high X-ray-to-optical flux ratios (van den Berg et al. 2009). Our observations of the LW using the IMACS camera on the Magellan 6.5 m telescope show one or two candidate counterparts within the error circle of six sources, and all show relatively high X-ray-to-optical flux ratios. The observed periods ($\sim$ 1.3 to 3.4 hours) and the X-ray luminosities ($10^{31.8-32.9}$ erg s^{-1} at 8 kpc) of the 10 periodic sources, combined with the lack of bright optical counterparts and thus high X-ray-to-optical flux ratios, suggest that they are likely accreting binaries, in particular, magnetic cataclysmic variables (MCVs). All of the 10 sources exhibit a relatively hard X-ray spectrum ($\Gamma < 2$ for a power law model) and X-ray spectra of at least five show an extinction larger than the field average expected from the interstellar medium in the region. The latter implies some intrinsic absorption in the system, which is also a typical sign of MCVs. The discovery of these periodic X-ray sources in the LW further supports the current view that MCVs constitute the majority of low luminosity hard X-ray sources ($\sim 10^{30-33}$ erg s^{-1}) found in the Bulge. The period distribution of these sources resembles those of polars, whereas the relatively hard spectra suggest that they could be intermediate polars (IPs). These puzzling properties, which are also shared by some of the periodic X-ray sources found in the Sgr A* field (Muno et al. 2003b), can be explained by unusual polars with buried magnetic fields or a rare sub-class of MCVs, nearly synchronous MCVs. These unusual MCVs may provide important clues in the evolutionary path of MCVs from IPs to polars. While the *Chandra* X-ray band appears relatively more sensitive in discovering these unusual MCVs, the completeness simulation indicates $\gtrsim$40% of the hard X-ray sources in the LW are periodic. Therefore, this discovery provides a first direct evidence of a large MCV population in the Bulge.

Subject headings: Galaxy: bulge — X-ray: binaries — cataclysmic variables

1. INTRODUCTION

The high sensitivity and superb spatial resolution of *Chandra* enabled population study of low-luminosity X-ray sources ($L_X \sim 10^{30-34}$ erg s^{-1}) on Galactic scales beyond the local solar neighborhood. Several ongoing campaigns, including our own *Chandra* Multi-wavelength Plane (ChaMPlane) survey (Grindlay et al. 2005) aim to improve the census of the Galactic low-luminosity X-ray sources. The Galactic Bulge, in particular, has been of great interest. More than 3000 discrete X-ray sources have been discovered in the $17' \times 17'$ region around Sgr A* (Muno et al. 2003a, 2009, hereafter M03a, M09). In ChaMPlane, we study the Bulge through our dedicated surveys of low-extinction bulge regions ("Windows survey") and a latitudinal strip around the Galactic center ("Bulge Latitude Survey"), where thousands of X-ray sources have been also discovered (Grindlay et al. 2011; Hong et al. 2009b, hereafter H09b). Multi-wavelength follow-up of these X-ray sources has been ongoing for source classification through optical/infrared imaging and spectroscopy (e.g. Koenig et al. 2008; van den Berg et al. 2006, 2009, hereafter B06, B09).

H09b (see also M03a) have found that the X-ray sources in the Galactic center region (GCR) show largely homogeneous X-ray properties (e.g. intrinsically hard X-ray spectra, photon power law index $\Gamma < 1$ for a power law model). The lack of bright IR (K<15) counterparts for the GCR X-ray sources indicates that HXMBs, once considered as a major constitute for Bulge X-ray sources, cannot account for more than 10% of the population (Laycock et al. 2005, hereafter L05). Currently the leading candidates that fit the observed properties are magnetic cataclysmic variables (MCVs) (L05; M09; H09b).

Recently we started a search for periodic ChaMPlane sources (e.g. Hong et al. 2009a, hereafter H09a), in part, to circumvent difficulties in source identification, which arise from large distances, high extinction (except for the Windows fields), and source confusion due to high stellar density in the Bulge. In this work, we report the discovery of 10 periodic X-ray sources from the 1 Ms *Chandra* exposure of the Limiting Window (LW), a low extinction region at 1.4° south of the Galactic center (see also H09b).

The low extinction Window fields, including the LW, provide a rare opportunity of studying the GCR source population without obscuration from molecular clouds (H09a,H09b,B06,B09). Revnivtsev et al (2009, hereafter R09) showed that the Galactic Ridge X-ray Emission (GRXE), the nature of which has been puzzling for decades, is mainly made up of discrete faint sources of known nature, primarily active binaries (ABs) or cataclysmic variables (CVs), based on the *Chandra* observations of the LW. However, the

* Send requests to J. Hong at jaesub@head.cfa.harvard.edu
[1] Harvard-Smithsonian Center for Astrophysics, 60 Garden St., Cambridge, MA 02138
[2] Utrecht University, 3508 TC Utrecht, The Netherlands

TABLE 1
Chandra ACIS-I OBSERVATIONS OF THE LW

Obs. ID	Start Time (UT: y/m/d h:m)	R.A. (°)	Decl. (°)	Roll (°)	GTI[a] (ks)	Exposure (ks)	Epoch[b] (duration)
6362	2005/08/19 16:15	267.86875	-29.58800	273	37.4	38	
5934	2005/08/22 08:16	267.86875	-29.58800	273	36.1	41	
				subtotal	*73.5*	*79*	*1 (3.13 d)*
6365	2005/10/25 14:55	267.86875	-29.58800	265	20.4	21	
				subtotal	*20.4*	*21*	*2 (0.24 d)*
9505	2008/05/07 15:29	267.86375	-29.58475	82	10.7	11	
9855	2008/05/08 05:00	267.86375	-29.58475	82	55.3	57	
				subtotal	*66.0*	*68*	*3 (1.22 d)*
9502	2008/07/17 15:45	267.86375	-29.58475	281	161.7	167	
9500	2008/07/20 08:11	267.86375	-29.58475	280	158.6	165	
9501	2008/07/23 08:13	267.86375	-29.58475	279	130.0	135	
9854	2008/07/27 05:53	267.86375	-29.58475	278	22.4	25	
9503	2008/07/28 17:37	267.86375	-29.58475	275	99.5	103	
9892	2008/07/31 08:07	267.86375	-29.58475	275	64.8	65	
9893	2008/08/01 02:44	267.86375	-29.58475	275	41.4	45	
9504	2008/08/02 21:23	267.86375	-29.58475	275	122.8	127	
				subtotal	*801.2*	*832*	*4 (17.7 d)*

[a]The selected Good Time Interval (GTI) that is based on the lack of high background fluctuations ($< 3\sigma$). See Hong et al. (2005). [b]The observations are grouped into four separate epochs (durations given in days), so that the total span of each epoch does not exceed a month.

exact composition of the discrete sources in the GRXE still remains unresolved (see also Revnivtsev et al 2011). We explore the X-ray and optical properties of the 10 periodic X-ray sources in the LW and their implication for evolutionary models of MCVs and their connection to thousands of X-ray sources in the GCR.

2. X-RAY OBSERVATION AND TIMING ANALYSIS

2.1. *Chandra Observation and Source Search*

The LW was observed for a total of 1 Ms exposure (100 ks in 2005 and 900 ks in 2008) with the *Chandra* ACIS-I instrument (H09b; R09). Table 1 lists the observational history of the field. The X-ray data were analyzed as a part of our ongoing ChaMPlane survey (Grindlay et al. 2005) and the analysis procedures are described in detail in Hong et al. (2005, hereafter H05; see also H09b). In summary, we stacked all of the 13 separate pointings and searched for discrete sources in the 0.3–2.5, 2.5–8.0, and 0.3–8.0 keV band images, using the *wavdetect* routine (Freeman et al. 2002). The source lists of the three energy bands were then cross checked to produce a list of 1397 unique discrete sources based on the positional uncertainty of each source. Carefully designed aperture photometry (H05) that takes into account source crowding was applied to each source in the 0.5–2.0, 2.0–8.0, and 0.5–8.0 keV bands. The complete source list and their photometries will be presented elsewhere (Hong et al. 2011) along with comparison of the results from two popular source detection algorithms, *wavdetect* and *wvdecomp*[3]. In this paper, we use the sources discovered by the *wavdetect* routine. Since we can identify periodic X-ray modulation only from relatively bright sources, the two search algorithms make no difference for the results of this paper. The catalog of the 319 sources and their photometry results from the initial 100 ks exposure can be found in H09b.

2.2. *X-ray Timing Analysis*

The 1 Ms *Chandra* exposure of the LW can be divided into into four epochs so that the total span of each epoch does not exceed a month, which allows period search in a single ephemeris (Table 1). Of four epochs, the last epoch provides a long exposure (GTI: 801 ks) suitable for in-depth search of periodic modulation. For periodicity search, we selected the 381 sources with background-subtracted net counts greater than 100 in the 0.3–8.0 keV band in Epoch 4 (Fig 1).

Photon arrival times of each source were Barycenter corrected to Barycentric Dynamical Time (TDB) by the `axbary` routine in the CIAO tool (ver 3.4). Then, we generated a background-subtracted light curve of each source in 12.8 s bins, and we applied a Lomb-Scargle (LS) routine (Scargle 1982) to the light curve to search for periodic X-ray modulation. We subtracted the background counts in the source aperture region using the events, with a proper scale, that fell in the background annulus region around the source, which excludes the source regions of neighbors (H05). The 12.8 s bin interval was chosen for efficient executions of the LS routine over a long exposure, and it only suppresses short periods below $\sim$ 100 sec (see §6.1 and Fig. 7), where there is already a concern due to the CCD readout time ($\sim$ 3.2 s). Randomization of photon arrival times to compensate for fixed CCD readout cycle makes practically no difference for the search results due to the longer time bins used for the light curves and the long exposure consisting of multiple pointings, where multiple phases of CCD readout cycle produces an effect similar to randomizing arrival times to some degree.

The search periods were selected successively, starting from the total duration (T) down to $10^{-4}T$ by a decrement of $\Delta P = P^2/(2Ts_f)$, where we introduced an oversampling factor, s_f (s_f=1 means no oversampling), in order to sample the periodograms relatively smoothly over the entire period search range. We change s_f logarithmically from 1.0 at the shortest period ($10^{-4}T$) to 4.0 at the longest (T), and a relative increase in the number of search periods due to the introduction of s_f is about 30%. In Epoch 4 where the total duration spans about 17.7 days with a combined total exposure of 832 ks, we searched 26499 periods from about 153 s

[3] By A. Vikhlinin; `http://hea-www.harvard.edu/RD/zhtools/`. See also M09.

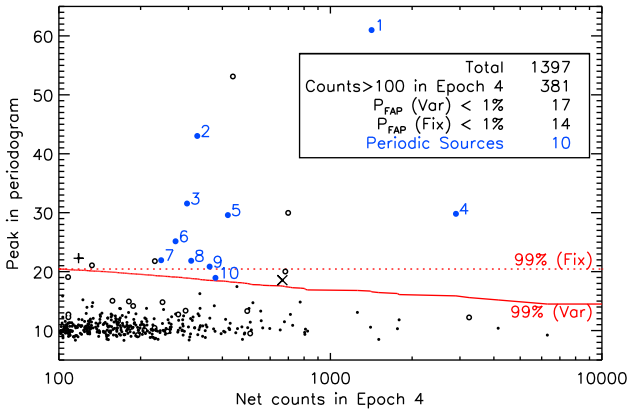


FIG. 1.— The distribution of the background subtracted counts in Epoch 4 of the sources and the peak values of the periodograms by the LS method. Of 17 sources with $P_{\rm FAP}$ (Var) $< 1\%$ (net count dependent False Alarm Probability; see §2.3 for its definition) or $P_{\rm conf}$ (Var) $> 99\%$ (red solid), we identify 10 periodic sources (see §3). The periodicities of 5 sources (open circles) are false, originating from either the dithering motion of the instrument or non-periodic X-ray variabilities (e.g. flares). We also exclude two other sources ('+' and 'x') because of the marginal nature of their detections (see §3).

to 17.7 days. In this analysis, we further limit the search range between 153 s and 10 hr, which contains 19911 independent periods out of 26247 trial periods. This range covers most of the spin and orbital periods of MCVs. We found that apparent periodicities of > 10 hrs indicated by the periodograms are false alarms, usually caused by short or long term X-ray variabilities (e.g. flares). For selected periodic sources (§2.3), we also extended the period search range down to 20 s in attempt to find any secondary modulation at periods shorter than 153 s, although the bin size (12.8 s) of the light curves may suppress detection of short periods below ~ 100 s (see Fig. 7).

For candidate periodic sources, we also applied an Epoch Folding (EF) method (Leahy et al. 1983) to refine the periods and compare the significance of the primary periods with their harmonics. For the EF method, we generated a background-subtracted folded light curve in 15 bins for a given search period and calculated the χ^2 value of the folded light curve with respect to the assumed constant count rate of no periodicity. For each source, we applied the EF method at 1000 periods within 2 σ of the primary period found by the LS routine, and the same around the half, 2nd and 3rd harmonics of the primary period.

2.3. *Periodic X-ray Source Selection*

In order to select valid periodic sources, we have estimated a False Alarm Probability ($P_{\rm FAP}$) or a confidence level ($P_{\rm conf} \equiv 1-P_{\rm FAP}$). For a given power density (X) in the LS routine, $P_{\rm FAP} = 1-(1-e^{-X})^{N_S N_P}$, where N_P is the number of independent trial periods (19911) and N_S is the number of the sources. To validate $P_{\rm FAP}$ estimated from the above trial statistics, we have also performed $\sim$ 100,000 simulations by randomizing photon arrival times. These simulations allow reliable estimates of $P_{\rm FAP}$ down to $\sim 0.1\%$ for $N_S \lesssim 10$ or $\sim 1\%$ for $N_S \lesssim 100$, etc., where the simulation results match with those from the trial statistics. For a larger value of N_S or a smaller value of $P_{\rm FAP}$, more simulations are required. In the following, we calculate $P_{\rm FAP}$ according to the trial statistics.

The search is usually conducted for the brightest sources first, since they have a better chance of periodicity detection. Depending on the search limit of net count ($N_{\rm net}$), which determines N_S, $P_{\rm FAP}$ changes. Although the LS routine is known to be more sensitive to low count sources than a few other conventional Fourier analyses (e.g. see Chapter 6.1 in Brethorst 1988), its performance eventually drops out as the net count decreases to zero. Extending the search limit by including low count sources with no chance of periodicity detection can arbitrarily increase $P_{\rm FAP}$, which can make valid periodic modulation appear insignificant. On the other hand, since search performance depends on various factors (e.g. background counts) besides net counts, it is desirable to extend the search to a relatively low net count to be conservative. Therefore, we set the search limit at a relatively low value ($N_{\rm net} = 100$), and we use two types of the $P_{\rm FAP}$ estimates: $P_{\rm FAP}$ (Var), where $N_S = N_S(\geq N_{\rm net})$, and $P_{\rm FAP}$ (Fix), where $N_S = N_S(N_{\rm net} \geq 100) = 381$. The former provides an initial cut for candidate periodic sources, and the latter provides a list of sources with a higher confidence.

Modulation amplitude is also a good metric for significance of periodicity. In order to describe diverse pulse profiles, we use the *rms* amplitude ($A_{\rm RMS}$) given by

$$A_{\rm RMS} = \left(\frac{Z_1^2}{N}\right)^{1/2} \frac{N}{N-B}, \quad (1)$$

$$Z_1^2 = \frac{2}{N}\left\{\left[\Sigma_j \cos\phi(t_j)\right]^2 + \left[\Sigma_j \sin^2\phi(t_j)\right]^2\right\}, \quad (2)$$

where N and B are the total and background number of events in the source aperture region respectively, and t_j is the arrival time, and $\phi(t)$ is the phase at time t that would be expected for a given period (Muno et al. 2003b, hereafter M03b and the references therein). For easy comparison with the literature, we also define another modulation amplitude as $A_M = 1-R_{\rm min}/R_{\rm max}$, where $R_{\rm min}$ ($R_{\rm max}$) is the minimum (maximum) count rate of the folded light curve. Finally, for synthetic light curve simulations, we use sinusoidal variations, where the light curve is described as $1+A_0\sin\phi(t)$, where $0 < A_0 \leq 1$ and $\phi(t)$ is the phase of photon arrival time t. For sinusoidal modulations, $A_0 = \sqrt{2}A_{\rm RMS}$, $A_M = 2\ A_0/(1+A_0)$, and $A_{\rm RMS} < A_0 \leq A_M$. Since both $R_{\rm min}$ and $R_{\rm max}$ depend on the bin size of folded light curves, we calculate A_M from $A_{\rm RMS}$ using the above relations.

We also use simulations to calculate a detection probability of periodicity ($P_{\rm det}$). For each candidate periodic source, we generate 1000 synthetic light curves to estimate $P_{\rm det}$ within about 1% accuracy. Each synthetic light curve is consistent with a sinusoidal variation of the measured period and modulation amplitude of the source, while accounting for the GTIs and Barycentric shifts of the CCD readout time of the real data. Then we perform the LS search algorithm to see how often we detect the same periodicity with $P_{\rm FAP}$ (Fix) $\leq 1\%$. These simulations enable completeness correction of periodicity detection (see also §6.2) and provide another validity measure of the detection in addition to $P_{\rm FAP}$.

Finally, we also performed the Bayesian Block (BB) search for long term variability (Scargle 1998). In order to apply the BB search to the data set of a long duration (3 yr) with long exposure gaps (>1 yr), we eliminate exposure gaps longer than 20 ks, and generate a semi-contiguous series of photon arrival times.

The simulations for $P_{\rm FAP}$ and $P_{\rm det}$ along with period search require significant computational power. In order to handle the computational burden efficiently at low cost, we have uti-

TABLE 2
PERIODIC SOURCES IN THE LW

(1) ID LWP	(2) Source Name CXOPS	(3) Counts (Epoch 4) (0.3–8 keV)	(4) Period (s)	(5) $P_{\rm FAP}$ (Fix) (10^{-n})	(6) $A_{\rm RMS}$ (%)	(7) $P_{\rm det}$ (%)	(8) Offset ($'$)	(9) Signi. Harmonics	(10) Notes
1	J175151.2-293310	1418(41)	10342(5)	19.6	26(3)	99.8	5.6		
2	J175123.5-293755	323(21)	5131(5)	11.8	59(5)	99.9	2.6		
3	J175129.1-292924	296(22)	7448(10)	6.8	65(6)	99.1	6.1		
4	J175131.6-292956	2899(56)	8536(14)	6.1	14(2)	83.3	5.6		BB:4
5	J175133.9-292754	419(29)	6342(7)	6.0	43(4)	67.5	7.7		
6	J175118.7-293811	269(19)	4729(2)	4.0	50(5)	80.1	3.3		
7	J175122.7-293436	†119(13)	12076(91)	2.6	60(8)	25.7	1.5	2	Edge: 352 ks
8	J175147.4-294215	307(28)	4890(6)	2.4	40(4)	9.6	7.9		
9	J175133.6-293313	359(21)	6597(10)	2.1	39(5)	66.1	2.6	3	PO:0.91
10	J175119.4-293659	377(22)	‡5262(2)	1.4	30(5)	13.9	2.4	2	2nd harmonic

(1) An abbreviated X-ray source ID. (2) The *Chandra* source name. (3) The background subtracted net counts in the 0.3–8 keV band in Epoch 4 (832 ks exposure). †The counts for LWP 7 is from the last 352 ks GTI, which is free of near CCD edge events (see §5.7). See Table 3 for the total net counts of the 1 Ms exposure. (4) The modulation periods are refined by the EF routine around the significant periods found by the LS routine. ‡For LWP 10, the second harmonic (5262 s) is considered the real period (see §5.10). (5) The False Alarm Probability for N_S=381 (see §2.3). (6) The *rms* modulation amplitude based on Eq. 1. (7) The detection probability of periodicity based on simulations using 1000 synthetic light curves for each source. (8) The offset from the aimpoint of Obs. ID 5934 (R. A.: 17h 51m 28.50s, DEC.: -29° 35′16.80″), (9) The most significant harmonic according to the EF method if the primary period is not. In LWP 10, the second harmonic is significantly more prominent than the primary primary (see §5.10), whereas in the other two sources, the differences are marginal. (10) BB: the number of independent Bayesian Blocks in the light curve if not one (see §5.4). Edge: the source falls near a CCD edge in some pointings and GTI free of such pointings is shown. PO: the 95% PSF overlaps with neighbors. The number indicates the fractional radius of the non-overlapping region (H05).

lized a GPU-based desktop supercomputer equipped with a C1060 Tesla GPU (240 cores) from Nvida[4]. A simple code conversion using an IDL[5] GPU library (*gpulib*[6]) has boosted the speed of some routines by a factor of 10 by comparison to the regular IDL routines[7].

3. X-RAY ANALYSIS RESULTS

Fig. 1 illustrates the search results and the periodic source count. For initial screening, we select 17 sources that exhibit a periodicity with $P_{\rm FAP}$ (Var) less than 1%. We exclude five sources with apparent periodicity due to either the dithering motion of the telescope (707, 1000 s and their immediate (sub-) harmonics), or non-periodic variabilities (e.g. flares). In addition, we exclude J175055.5-292948 (period: 5331 s) since its $P_{\rm det}$ is only 0.1% ('+' in Fig. 1). For sources with $P_{\rm FAP}$ (Fix) $\geq$ 1%, we only consider them periodic if they show another significant indicator of periodicity (e.g. the results of the EF method, see §5.10), and so J175103.9-293430 (period: 3821 s) is also excluded ('x' in the figure). The final list of the periodic sources in the LW contains 10 sources (9 with $P_{\rm FAP}$ (Fix) $<$ 1%). The spatial distribution of the 10 periodic sources does not show any obvious sign of clustering or pattern.

Table 2 lists the basic results of period search and photometry of the 10 periodic sources in the LW. For easy reference, in addition to the X-ray source name (starting with CXOPS, see H05), we assign an abbreviated version of the name starting with prefix 'LWP' indicating 'Limiting Window Periodic sources'. The number IDs in the short name are assigned in the reverse order of the periodogram value at the observed periods (i.e. the likelihood of true periodicity). Note B09 list the sources with prefix 'LW'.

[4] http://www.nvidia.com
[5] http://www.ittvis.com/idl
[6] http://txcorp.com/products/GPULib
[7] The complete code optimization is expected to boost the speed by another factor of 10 according to the examples given by *gpulib*.

Figs. 2 and 3 show the periodograms, the folded light curves, the X-ray spectra with model fits, and the compressed light curves without long exposure gaps of the 10 periodic sources. The periodograms are based on the LS method, which was applied to the binned light curves of Epoch 4. The folded light curves are also generated from the data obtained in Epoch 4 and are very similar to the ones from the full 1 Ms exposure (not shown). The periodogram and the folded light curve of LWP 7 are from the last 352 ks GTI in 8.1d when the source was observed sufficiently distant of any CCD edges.

The X-ray spectrum of each source is generated using all of the available data, and each spectral bin contains more than 20 background-subtracted net counts. The red solid lines show the results using a simple power model fit, and for LWP 1, a spectral fit using a power law plus an iron line at 6.7 keV is also shown (blue). In the compressed light curves, the long exposure gaps ($>$ 20 ks), are marked by the vertical lines, and the yellow lines indicate the boundaries of four epochs. The red horizontal lines show the average count rate and the green lines show the effective area, which varies from pointing to pointing. The blue solid lines for LWP 4 show the count rates of the BBs.

Table 3 summarizes the X-ray spectral properties including estimates of the unabsorbed X-ray fluxes, based on spectral model fits. Note the net counts in Table 3 are from the full 1 Ms exposure, whereas the net counts in Table 2 are from Epoch 4 except for LWP 7, which shows the net count from the last 352 ks GTI. We fit the spectra of all the sources using a simple power law model, and for LWP 1, we also tried a power law plus an iron line (see §5.1).

4. OPTICAL OBSERVATION AND PROPERTIES

We observed the LW field with the *HST* and Magellan telescope. Five of the 10 sources were in the *HST*/ACS fields (B09), and three of them were reported as possible candidates for accreting binaries or CVs. Table 4 summarizes the combined optical and X-ray properties of the candidate optical

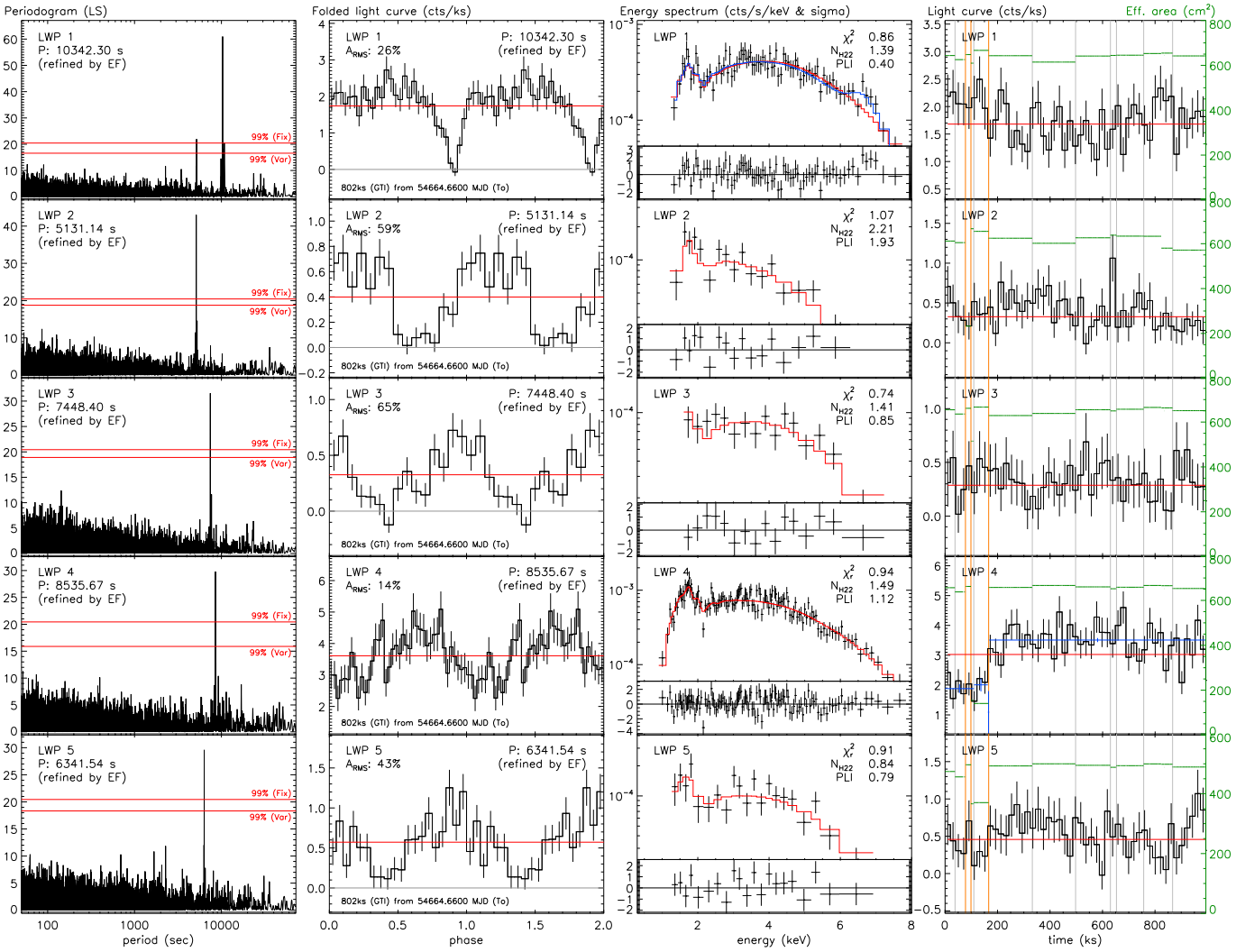


FIG. 2.— Periodograms, folded light curves, energy spectra and compressed light curves of the periodic X-ray sources (LWP 1–5) in the LW. The periodograms are based on the LS method, and the 99% confidence levels for $N_S = 381$ (Fix) and $N_S = N_S(> N_{\rm net})$ (Var) are shown in (red) horizontal lines (see §2.3). The folded light curves are drawn with T_0 = MJD 54664.6600, and the (red) horizontal lines show the average rates. In the energy spectra, the (red) lines show the results of simple power law model fits. In the case of LWP 1, a model fit using a power law plus an iron line is shown in blue. In the compressed light curves, the (red) horizontal lines represent the average rate, the (green) steps show the effective area of each pointing, and the vertical lines indicate the epoch boundaries (yellow) and exposure gaps (grey, > 20 ks). For LWP 4, the Bayesian Blocks are shown in blue lines.

counterparts of the *Chandra* sources. For easy reference, the short names used by B09 are noted for the three sources in Table 4 (e.g. LWP 2 = LW 25).

4.1. *HST/ACS Data and Analysis*

We observed with *HST* the inner area of the ACIS field with a 2 ×2 mosaic of the Wide Field Camera (WFC) on the ACS on 2005 August 19. A single WFC pointing images a $3.4' \times 3.4'$ field with $\sim 0.05''$ pixels using two CCD detectors separated by a $2.5''$ gap. Exposures were taken through the F435W (B_{435}), F625W (R_{625}, similar to Sloan r), and F658N (Hα) filters. Each tile of the mosaic was observed with the same exposure sequence 4 ×492 s in F435W, 168 s + 2 ×167 s in F625W, and 4 ×496 s + 4 ×492 s in F658N. No dithering was applied to fill in the WFC chip gap. Photometry is performed using a stellar-photometry package, DOLPHOT, a modified version of the HSTphot package to do photometry on HST/WFPC2 images (Dolphin 2000). See B09 for the details.

4.2. *Magellan/IMACS Data and Analysis*

On 2007 May 8, we observed the LW field and two other Window fields (Stanek's and Baade's) with the Inamori Magellan Areal Camera and Spectrograph (IMACS) on the 6.5 m Magellan (Baade) telescope at Las Campanas, Chile. With seeing $\sim 0.8-1.2''$ FWHM, we obtained a dithered set of 5 pointings in the f/4 configuration ($15.4'$ field, $0.11''$/pixel) to cover an $18' \times 18'$ region of the LW. This provided a total exposure time of 600, 300, 180, & 180 s in Bessell-B, V, R, & CTIO-I filters over the *Chandra* field respectively.

We processed the images using standard IRAF tasks, and calibrated the astrometry using the 2MASS catalog as a reference. The astrometric residuals on each CCD frame were $\sim 0.2''$. We reprojected and stacked the images using the SWARP[8] utility. All frames were normalized to ADU/second units and combined using weight-maps constructed from flat-fields and bad pixel masks. The initial source search and

[8] http://www.astromatic.net/software/swarp

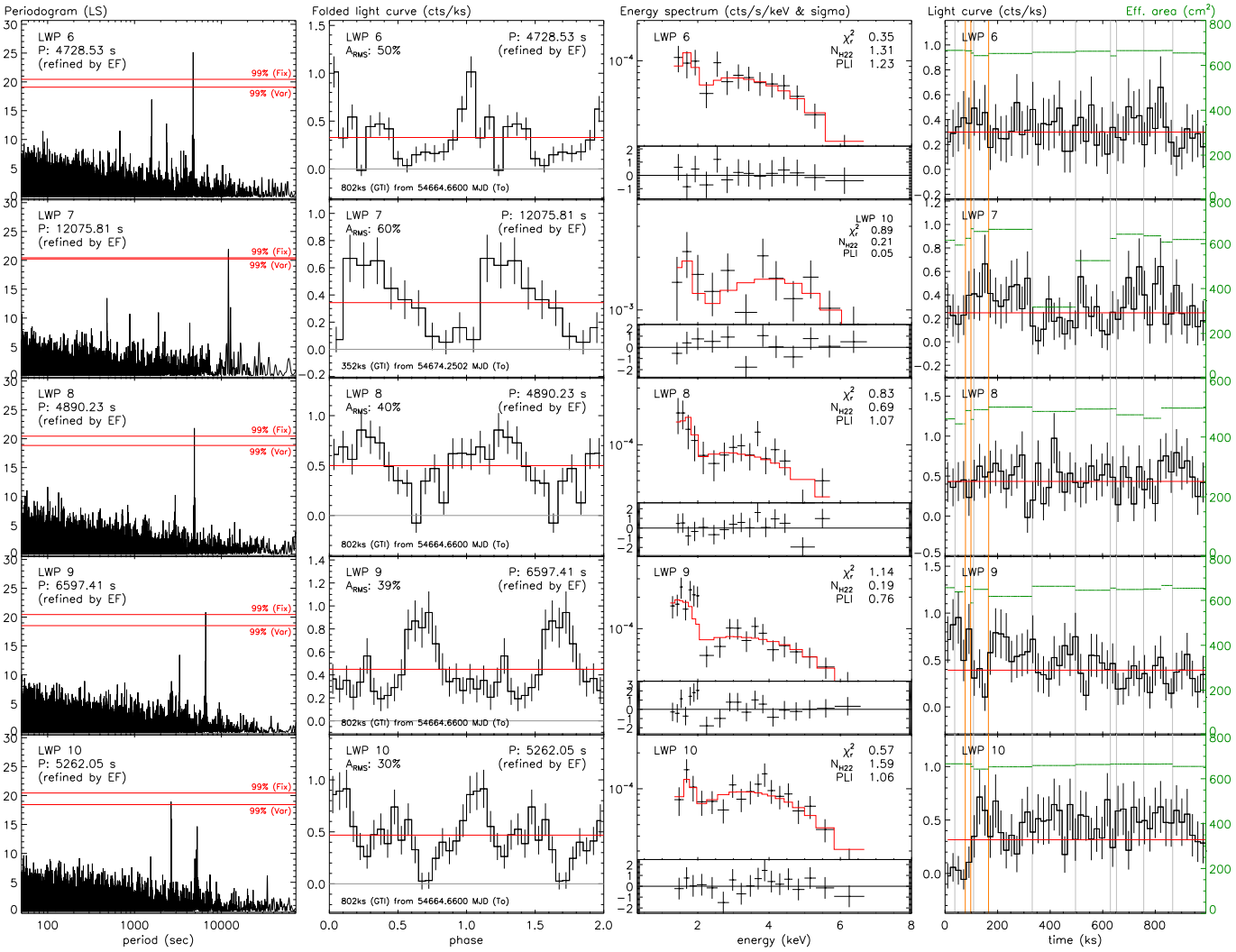


FIG. 3.— Same as Fig. 2 for LWP 6–10. The folded light curve of LWP 7 is drawn with T_0 = MJD 54674.2502.

photometry were performed on the stacked images using DAOPHOT. See also H09a.

4.3. *Optical Matches*

Both the *HST* and IMACS source lists are boresighted to the *Chandra* sources as described in Zhao et al. (2005): the boresight correction is less than 0.1″ in both R. A. and Declination. In search of optical counterparts and their optical properties, for the five sources in the *HST*/ACS fields, we use the *HST* observations. For the other five, we use the Magellan/IMACS observations, where three sources show one or two candidate counterparts. Considering the high stellar density in the region, there is no guarantee of these Magellan/IMACS sources being the true counterparts (e.g. LWP 9 has six candidate counterparts seen in the *HST*/ACS field, but only one in the Magellan/IMACS image).

The X-ray-to-optical flux ratios, Log(F_X/F_R), in Table 4 are calculated for the 0.3-8 keV band vs. the *R* magnitude. Both the observed and unabsorbed flux ratios are given. For unabsorbed flux ratios, the *R* magnitude is de-reddened based on the A_{F625W} map given by Revnivtsev et al (2010). For sources with multiple candidate counterparts, a range of the *R* magnitude and the flux ratio is given, covering all the candidate counterparts. In the case of LWP 2 (= LW 25) and LWP 6 (= LW 8), shown is the *R* magnitude of the most likely candidate with an unusually blue color (B09). In the case of LWP 8, only one of the candidate counterparts has a measurable *R* magnitude. For sources with no detectable candidate counterparts, a lower limit for the *R* magnitude is given, based on the minimum value of optical neighbors within a 30″ radius of the X-ray source position.

The logarithmic flux ratios or their limits of these periodic sources are relatively high: > -1 for 7 sources and > -2.5 for the rest. The intrinsic X-ray-to-optical flux ratios of accreting binaries or AGN are usually significantly higher than those of coronal sources (see §4.1.2 in B09 and the references therein). CVs have the intrinsic flux ratio between −2.5 and +0.5 in the above energy bands, although a few outliers of active binaries or dMe stars have the flux ratios as high as −1 or −0.5. Therefore, the flux ratio results in Table 4 are consistent with those of CVs.

Note that, except for a few cases with an outstanding blue counterpart, most of the flux ratio values in Table 4 are in fact likely lower limits, considering the high stellar density in the

TABLE 3
X-RAY SPECTRAL PROPERTIES OF THE PERIODIC SOURCES IN THE LW BASED ON SIMPLE POWER MODEL FITS

(1) Source ID LWP	(2) Counts (Total) (0.3–8 keV)	(3) E_{50} (keV)	(4) N_{H22}	(5) Γ	(6) EW (keV)	(7) χ^2_ν/DoF	(8) Unabsorbed Flux 0.5–2 (10^{-15} erg cm^{-2} s^{-1})	2–8	0.3–8 keV	(9) Luminosity 0.3–8 keV (10^x erg s^{-1})
1	1775(45)	3.86(6)	1.4(2)	0.4(1)		0.86/74	6.3(5)	56(2)	63(2)	30.9 – 32.7
			1.7(1)	0.63(2)	0.5(1)	0.74/72	8.3(7)	55(1)	64(2)	30.9 – 32.7
2	393(23)	2.9(1)	2.2(5)	1.9(3)		1.07/14	9(1)	8.9(6)	21(1)	30.4 – 32.2
3	361(24)	3.7(2)	1.4(9)	0.8(4)		0.74/13	1.4(4)	10.2(7)	12.0(8)	30.2 – 32.0
4	3217(59)	3.36(4)	1.5(1)	1.12(8)		0.94/123	24(1)	79(2)	107(2)	31.1 – 32.9
5	473(30)	3.4(2)	0.8(5)	0.8(3)		0.91/18	2.5(4)	12.7(9)	16(1)	30.3 – 32.1
6	329(21)	3.2(1)	1.3(6)	1.2(4)		0.35/11	2.6(4)	7.0(5)	10.0(6)	30.1 – 31.9
7	295(20)	3.8(1)	0.0(3)	0.0(1)		1.00/10	0.32(6)	7.8(6)	7.6(5)	30.0 – 31.8
8	361(30)	3.0(2)	0.7(8)	1.1(5)		0.83/13	1.9(4)	8.1(7)	10.3(9)	30.1 – 31.9
9	457(24)	2.9(1)	0.2(3)	0.8(3)		1.14/17	1.3(1)	8.0(5)	9.3(5)	30.0 – 31.9
10	415(23)	3.58(9)	1.6(5)	1.1(3)		0.57/15	3.1(4)	9.7(6)	13.1(7)	30.2 – 32.0

(1) An abbreviated X-ray source ID. (2) The background-subtracted net counts in the 0.3–8 keV band from the full 1 Ms exposure. (3) The median energy of the photons in the 0.3–8 keV band. (4) & (5) An estimate of the power law index (Γ) and the absorption (N_{H22}) from spectral model fits, assuming a simple power law model for the X-ray spectrum in the 0.3–8 keV band. (6) The estimated equivalent width of the iron line from a spectral fit of a power law model with an iron line at 6.7 keV. (7) Reduced χ^2 and Degree of Freedom (DoF) of spectral model fits. (8) An estimate of the unabsorbed flux. (9) The luminosity range in the 0.3–8 keV band for source distance at 1–8 kpc.

TABLE 4
CANDIDATE OPTICAL COUNTERPARTS OF THE PERIODIC SOURCES IN THE LW

(1) Source LWP	(2) R (mag)	(3) B-R	(4) F_X (0.3–8 keV) (observed)	(unabsorbed)	(5) Log(F_X/F_R) (observed)	(unabsorbed)	(6) No. of Candidates *HST*	Magellan	(7) A_{F625W} (offset)
1	>22.3		51(1)	64(2)	>1.4	>-0.1			3.9 (1.5′)
2	22.3 .. 24.4		8.0(5)	21(1)	0.6 .. 1.4	-0.4 .. 0.4	2 (LW25)		3.6 (0.1′)
3	>22.2		9.2(6)	12.0(8)	>0.6	>-1.0			4.2 (1.9′)
4	23.1(4)		75(1)	107(2)	1.9(2)	0.4(2)		1	4.1 (1.4′)
5	20.5(2)*		13.0(8)	16(1)	0.08(8)*	-1.47(8)*		1	4.1 (3.4′)
6	22.7(1)	2.9	6.8(4)	10.0(6)	0.68(5)	-0.72(5)	5 (LW8)	1	3.9 (0.3′)
7	18.8		7.6(5)	7.6(5)	-0.83(3)	-2.47(3)	1	1	4.1 (0.5′)
8	21.4(2)		8.1(7)	10.3(9)	0.23(9)	-1.02(9)		2	3.4 (3.5′)
9	22.4 .. 25.7		8.6(5)	9.3(5)	0.7 .. 2.0	-0.7 .. 0.6	6 (LW19)	1	3.6 (0.2′)
10	22.6 .. 24.6		9.3(5)	13.1(7)	0.8 .. 1.6	-0.6 .. 0.2	4		3.8 (0.1′)

(1) An abbreviated X-ray source ID. (2) *R* magnitude, based on the *HST* observation if available: otherwise, based on the Magellan Images. For sources with multiple counterparts, the range of those counterparts is given. For sources with no valid counterparts, a lower limit is given, based on the minimum magnitude of neighboring optical sources within a 30″ radius from the X-ray source position. '*' uses the *I* magnitude instead of *R*. (3) *B* (F435W) − *R* (F625W) from the *HST* observation. (4) The X-ray flux in 10^{-15} erg cm^{-2} s^{-1}, from column (7) in Table 3. (5) $\mathrm{Log}(F_X/F_R) = \mathrm{Log}(F_X) + R/2.5 + 5.76$. For unabsorbed flux ratios, the *R* magnitudes are de-reddened by A_{F625W}. (6) The number of candidate counterparts found in the Advanced Camera for Surveys (ACS) images of the *HST* and the Magellan MOSAIC Images. Every source in the ACS FoV has more than one counterpart and for sources reported by B09, their source IDs are given. (7) A_{F625W} from Revnivtsev et al (2010) and the offset of the source from where A_{F625W} is sampled.

region and the possibility of the true counterpart being fainter and undetected. LWP 5 and 8 have additional uncertainties in their estimates due to the variation in the interstellar absorption across the region: for these sources, the A_{F625W} values were sampled about 3 or 4′ away from the sources. For LWP 7 and 9, the absorption in the X-ray spectra is estimated less than what is expected in the field, based on A_{F625W}. For LWP 3, 5 and 8, two estimates are consistent, and for the rest, the former is larger than the latter.

5. SOURCE PROPERTIES

In this section, we discuss some of the unique properties or analysis caveats of each source.

5.1. *LWP 1: CXOPS J175151.2-293310*

The periodogram reveals significant periodic modulation at the primary period and its half. The folded light curve shows a clear eclipse, but due to the lack of other features in the folded light curve other than the eclipse, the system can be either a polar or an IP. The long period suggests the modulation is likely due to the orbital motion (e.g. only two IPs with $\gtrsim 10^4$ s spin period in Fig. 6a, see §6.1 for the details). If so, the mass of the companion is estimated to be $\sim 0.42\ M_\odot$ according to Eq. 2.89 in Warner (1995). In addition, from the eclipse duration $\Delta\phi \sim 0.09$, the mass ratio $q \gtrsim 0.29$ and the inclination angle i is somewhere between 60° and 74° for white dwarf (WD) mass $M_1 \sim 0.1 - 1.4 M_\odot$ (Eq. 2.92 & 2.93 in Warner 1995).

The X-ray spectrum exhibits a feature consistent with an iron line at 6.7 keV (and perhaps 6.4 keV as well). The spectral fit with a power law plus a 6.7 keV line reduces the χ^2_ν by 14%, compared to a simple power law model (Table 3). In order to estimate the significance of the line (see Protassov 2002), we generated 1000 synthetic spectra, each of which is

consistent with a simple power law model ($\Gamma = 0.4$ and $N_{\rm H22} = 1.4$). We then fit each spectrum with a power law plus the iron line, and count how many cases reduce the χ^2_ν by more than 14%. The results were none, indicating the significance of the line is 99.9% or higher. The hard X-ray spectrum with an iron emission line suggests the source is likely an IP (see more about the source type in §6.1).

5.2. *LWP 2: CXOPS J175123.5-293755*

This source was reported as a possible accreting binary (LW 25) by B09. Two optical sources in the *HST*/ACS images are found within the error circle of the X-ray source position, and neither of them stands out with any unusual colors. The folded light curve shows a possibility of a long eclipse starting at phase ~ 0.5. LWP 2 and 6 are located in the region with an excess of seemingly diffuse soft X-ray background, which perhaps indicates the lowest extinction region of the field. In the case of LWP 2, it shows a significantly larger absorption in the X-ray spectrum than the field average, indicating an intrinsic absorption in the system.

5.3. *LWP 3: CXOPS J175129.1-292924*

This source exhibits a mild anti-correlation between the count rate and the absorption in the X-ray spectrum according to a phase-resolved quantile diagram (Fig. 4) (Hong et al. 2004, H09a). This anti-correlation is consistent with a picture that the observed X-ray modulation is caused by the variation of intrinsic absorption in the system, similar to the IP discovered in BW (H09a). Alternatively if the X-ray modulation originates from an eclipse or an obscuration of the hot spot or the emission region due to the spin or orbital motion, then the absorption variation may not be expected to be strongly correlated with the rate change. The folded light curve of the source shows a hint of an eclipse (phase ~ 0.45), which, if true, implies the system is sychronized (i.e. polar), considering the synchronized primary modulation in the folded light curve.

5.4. *LWP 4: CXOPS J175131.6-292956*

This is the brightest source of the 10 periodic sources. The X-ray spectrum does not show any sign of iron lines. The BB search indicated four independent blocks in the long term light curve, but since the source fell near a CCD edge in Epoch 3, only two blocks can be credited to be independent. In summary, the observed X-ray flux in 2008 is higher by a factor of ~ 1.8 than that in 2005.

5.5. *LWP 5: CXOPS J175133.9-292754*

This source and LWP 8 were observed at relatively large off-axis angles.

5.6. *LWP 6: CXOPS J175118.7-293811*

This source was reported as a candidate CV (LW 8) by B09, based on the high X-ray-to-optical flux ratio and Hα excess (see Fig. 4 in B09). The folded light curve in Fig. 2 shows a hint of an eclipse at phase ~ 0.2. Our routine analysis of phase-resolved quantiles at the primary period and the second harmonic revealed an intriguing result as illustrated in Fig. 5. At each period, we show two versions of folded light curves using sliding phase windows: one with fixed-width phase bins (10%, grey), and the other with variable-width phase bins but fixed net counts in each phase bin (45 counts, black). The former is better suited to identify a sudden drop in the count rate such as an eclipse, and the latter is better suited to reveal a sudden increase. In addition, the latter is better suited for phase-resolved spectral quantile analysis since every phase bin contains enough events to allow a reliable estimate of energy quantiles. The folded light curves in fixed-width phase bins show an eclipse-like feature both at the primary period (phase ~ 0.2 and 0.6) and at the second harmonic (~ 0.25). The ingress and egress of the eclipse are sharper at the second harmonic than the primary period. A narrow eclipse, synchronized with the primary modulation, suggests the system is a polar.

What is interesting in this source is a spectral change correlated with the phase. At the primary period, the first quarter of the phase shows an intrinsically harder X-ray spectrum ($\Gamma < 1$) than the rest ($\Gamma > 1$), which implies two different emission regions or mechanisms are present (Fig. 5e). On the other hand, at the second harmonic, there appears to be a dramatic change in the absorption between the first ($N_{\rm H22} \gtrsim 2$) and second halves ($N_{\rm H22} \lesssim 1$) of the phase (Fig. 5d & f). The change in the absorption between two peaks of the folded light curve would suggest that two magnetic poles of the system are visible in turn, and the X-ray emission from one of the two undergoes through more material (likely an accretion curtain, trailing to a pole and extended from about half of the accretion disk or ring) before reaching us. Fig. 5 in Evans & Hellier (2007) illustrates a possible viewing geometry for such a system: unlike their exmaples, the soft blackbody component ($\ll 1$ keV) of LWP 6 is likely always invisible due to the interstellar absorption, but the geometry allowing for a phase-dependent variation of intrinsic absorption due to an accretion stream or curtain can apply to LWP 6. This picture, if true, suggests that the second harmonic (9457 s) is a real period and the observed primary period (4729 s) is a sub-harmonic, even though the LS method did not find the second harmonic significant. Further observation is required to determine which period represents the true orbital and spin geometry. In addition, a new diagnosis may be required to quantitatively evaluate the significance of various types of spectral changes (see Connors 2011).

5.7. *LWP 7: CXOPS J175122.7-293436*

During three pointings out of 8 total in Epoch 4, this source fell near a CCD edge (see the effective area in Fig. 3), which would discredit the observed periodicity, but the relatively clean data set (the last 352 ks GTI) free of near-CCD-edge events also exhibits a significant periodicity at 12076 s. The net count of LWP 7 in the last 352 ks GTI is only 119, which is similar to that of J175055.5-292948 ('+' in Fig. 1) in Epoch 4, but $P_{\rm det}$ of LWP 7 is estimated substantially higher than J175055.5-292948 because of the relatively lower background counts in the source aperture region of LWP 7. Therefore, we consider the observed periodicity of LWP 7 valid.

5.8. *LWP 8: CXOPS J175147.4-294215*

The folded light curve of the source shows an eclipse-like feature at phase ~ 0.6.

5.9. *LWP 9: CXOPS J175133.6-293313*

LWP 9 was reported as a potential accreting binary (LW 19) by B09. The aperture source region (95% PSF) of these sources mildly overlaps with that of a neighbor. A clean data set relatively free of contamination from the neighbor (see

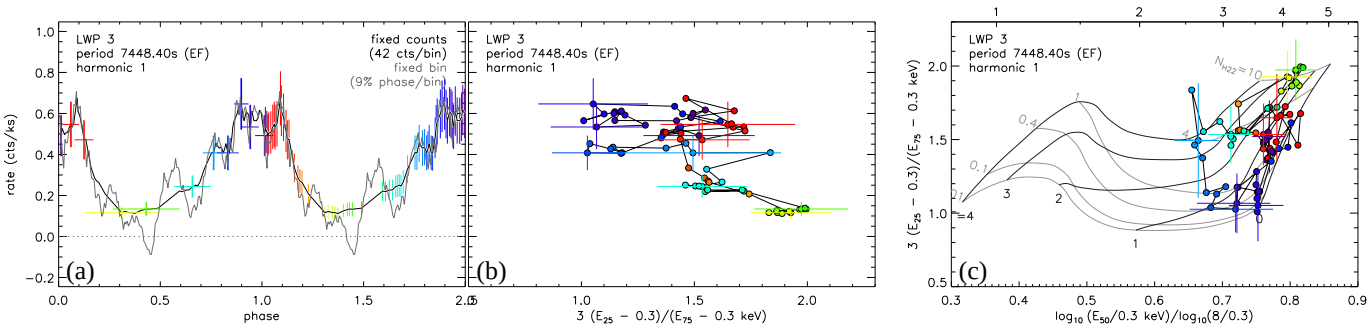


FIG. 4.— Phase-resolved quantile analysis of LWP 3 using the last 801 ks exposure: (a) the folded light curves, (b) the rate vs. the quartile ratios, and (c) the phase-resolved quantile diagram. The folded light curves are generated using sliding windows of fixed-width phase bins (grey) and variable width phase bins with fixed net counts (black: example data points with bin sizes are shown in phase 0 – 1) and the error bars of the latter are color-coded by phase for easy comparison. The quartile ratios is mostly proportional to Log($N_{\rm H22}$) for LWP 3.

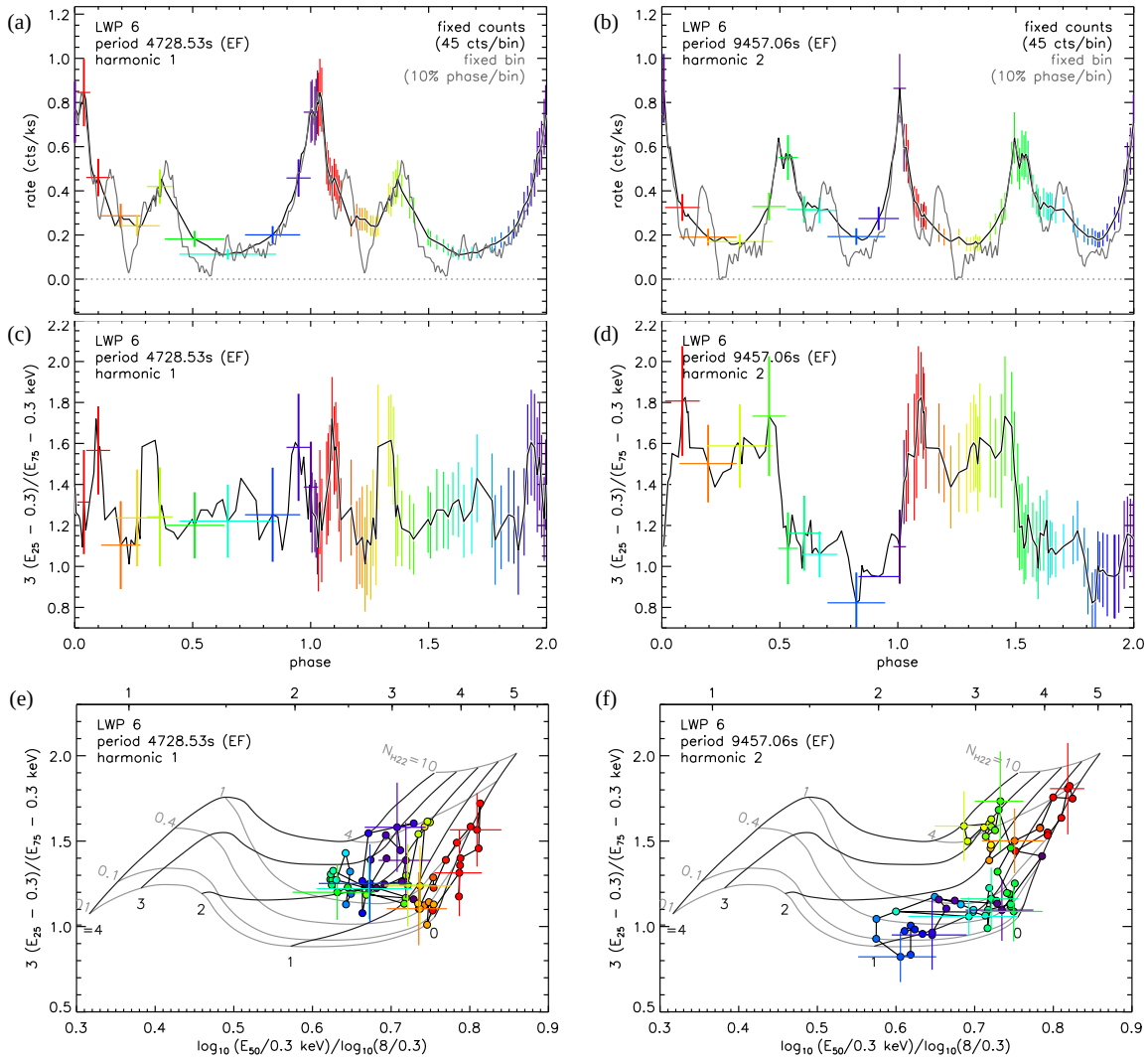


FIG. 5.— Phase-resolved quantile analysis for LWP 6: the left panels for the primary period (4731 s) and the right panels for the second harmonics (9461 s). (a,b) the folded light curves, (c,d) the phase-resolved estimates of $N_{\rm H22}$ using the power law models in the quantile diagram and (e,f) the phase-resolved quantile diagram. For the 9461 s period (d), the first half of the phase (0.0–0.5) shows a higher absorption ($N_{\rm H22} \gtrsim 2$) than the second half (0.5–1.0) ($N_{\rm H22} \lesssim 1$).

H05 for aperture choice) exhibits the same periodic modulation, so that its periodicity is considered valid.

5.10. *LWP 10: CXOPS J175119.4-293659*

According to the EF analysis for LWP 7, 9 and 10, a higher harmonic exhibits more significant periodicity than the primary period found by the LS method. While the differences in the significance between the primary periods and their harmonics are marginal for two sources, in the case of LWP 10 the second harmonic appears substantially more significant. The χ^2 of the 15-bin folded light curve with respect to the constant rate is 133 at the second harmonic vs. 89.5 at the primary period[9]. Therefore we consider the second harmonic to be the real modulation period for LWP 10. The high χ^2 value at the second harmonic is partially due to an eclipse-like feature in the folded light curve at phase ~ 0.7, which suggests the system is a polar.

6. DISCUSSION

In this section, we investigate the most probable source types for the periodic sources found in the LW and their implications, based on the statistical distribution of their properties. We also explore the hidden population of periodic sources in the Bulge X-ray sources in the GCR through completeness simulations for periodicity detection.

6.1. *Unusual MCVs?*

The observed source properties such as the X-ray luminosity range ($\sim 10^{30-33}$ erg s^{-1} for distance of 1 – 8 kpc), the relatively hard X-ray spectra ($\Gamma < 2$), the period range (1.3 – 3.4 hr), and the relatively high X-ray-to-optical flux ratios, all indicate that these sources are typical MCVs. But the collection of these properties does not appear to fit well with most common types of MCVs as explained below.

MCVs can be largely divided into two groups, IPs and polars, depending on the relative strength of the magnetic fields. Traditionally, polars are synchronized or nearly synchronous ($P_s/P_o \sim 0.98 - 1.02$), whereas IPs are not ($P_s/P_o \lesssim 0.1$). Fig. 6 shows the spin vs. orbital period distribution of the MCVs in the Ritter & Kolb (RK) catalog (ver 7.15) (Ritter & Kolb 2003). In Fig. 6a, the observed periods of the periodic X-ray sources found in the LW and Sgr A* fields are shown as orbital periods along $P_s/P_o = 2$ or 4 for easy comparison.

In the case of the periodic sources in the LW, the observed period distribution (red in Fig. 6b) resembles those of polars (green) better than either the spin (black) or orbital (blue) periods of IPs. Some IPs do have spin or orbital periods at around an hour to three hours, but the majority of the spin (or orbital) periods are shorter (or longer), whereas the majority of the periods of polars are in the same range as those of the periodic sources in the LW.

In order to find out if the above result is due to a period-dependent selection bias in the periodicity search routines, we have conducted a set of simulations using synthetic light curves with various net counts (100 to 1000), modulation amplitudes (A_0 = 10% to 100%) and periods ($\sim$ 20 to 1.1×10^5 s). For each combination of parameters, we generate 500 synthetic light curves, which allows $\lesssim 2\%$ accuracy in measurement of the detection probability. As in the simulations in §2.3 (and §6.2), each synthetic light curve is generated to properly reflect the GTIs and Barycentric shifts of the CCD readout time of the real data.

The simulation results show there is no significant selection bias in the range of 150 sec to 10 hr (Fig. 7). This implies that the resemblance to the polar period distribution is not due to any selection effect in the search algorithms[10], or if these sources are IPs, they indeed belong to a statistically different population from the typical IPs in the RK catalog. In addition to the observed eclipses (or eclipse-like features) synchronized with the primary modulation of the pulsed profiles (e.g. LWP 3, 6, 8 or 10), missing secondary periods from all the sources in Table 2 indirectly supports the systems being polars - synchronized systems, although non-detection does not guarantee the absence of the secondary periods.

Fig 8 illustrates a wide range of modulation amplitudes of the 10 periodic sources in the LW. For comparison, we also show some of literature-selected IPs and polars. If the X-ray emission originates from a small spot (e.g. polar cap) on the WD surface, the modulation due to the spinning motion of the compact object is expected to exhibit a larger amplitude change than that from the orbital motion. For instance, a sample of IPs in Fig. 8, selected from the literature, show a slightly higher average value of the modulation amplitude at the spin periods (black closed circles) than at the orbital periods (black open circles). However, the modulation distributions of these IPs and polars in Fig. 8 are likely selection biased: e.g. 17 polars in Fig. 8 are mostly eclipsing systems, which are likely preferentially found in periodicity searches due to the large modulation amplitude. Note for polars in Fig. 8, A_M is simply based on $R_{\rm min}$ and $R_{\rm max}$ of the published light curves, where by definition, A_M=1 for eclipsing systems, whereas for the periodic sources in the LW, we calculate A_M from $A_{\rm rms}$ (e.g. for LWP 1, A_M=0.53 instead of 1.0). In summary, it is not easy to link the distribution of the modulation amplitudes to a particular type of MCVs due to the lack of systematic survey. However, even in Fig. 8 with selected samples of IPs and polars, the period distribution of the 10 periodic sources strongly favors polars.

Unlike the period distribution, the relatively hard X-ray spectra of the periodic sources in the LW imply that these systems are likely IPs. The quantile diagrams in Fig. 9 illustrate the overall spectral hardness of the periodic sources (red) in comparison with the rest of the X-ray sources (black dots, net counts $\geq$ 50) in the LW. Fig. 9a and b overlay a set of simple power law and APEC model grids respectively over the same data points. The eight periodic sources found in the Sgr A* field are also shown in (green) crosses (M03b). All of the periodic sources show an intrinsically hard X-ray spectrum, similarly to the periodic sources in the Sgr A* field.

IPs tend to show harder X-ray spectra, which are associated with higher accretion rates and weaker magnetic fields (Ramsay & Cropper 2004). For instance, in the case of polars, the X-ray spectra are well described by a blackbody component with $kT < 60$ eV and a two-temperature thermal plasma component with $kT_1 = 0.7-0.9$ keV and $kT_2 = 3-5$ keV (e.g. Ramsay et al. 2004b), whereas the X-ray spectra of IPs show a blackbody component with $kT > 60$ eV and a one or two-temperature thermal plasma component with $kT \geq 10$ keV (e.g. Anzolin 2008). Due to the interstellar absorption in the LW field ($N_{\rm H22} \sim 0.7$), the blackbody component is usu-

[9] For comparison, the expected χ^2 of the 15-bin folded light curve is 70.9 at $P_{\rm FAP}$ = 1% for N_S= 381 and N_P=19911, although the EF search was conducted only for the 10 sources at 4000 periods around the likely true modulation periods.

[10] There is, however, a selection bias towards sources with high modulation amplitudes, as expected. See §6.2.

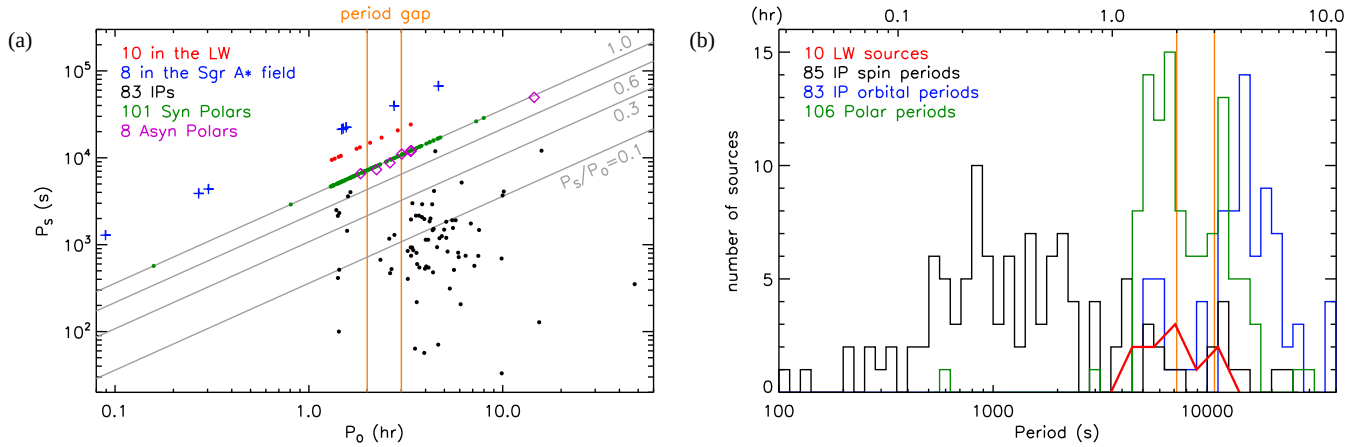


FIG. 6.— (a) The spin (P_S) vs. orbital period (P_O) distribution of MCVs from the RK catalog (ver 7.15). The vertical yellow lines mark the period gap, and the diagonal lines represent P_S/P_O = 1, 0.6, 0.3 and 0.1. The purple diamonds show eight asynchronous polars (APs) (three are on top of each other), and there are six near synchronous IPs with $P_S/P_O > 0.3$. The observed periods of the periodic sources in the LW (red) and the Sgr A* field (blue) are marked as orbital periods, along $P_S = 2\ P_O$ or $4\ P_O$ for clarity (those less than an hour are likely the spin periods). (b) The period distribution of the LW sources (red) is compared to the distribution of the spin (black) and orbital (blue) periods of IPs and the periods (green) of polars in the RK catalog. The periodic sources (red) in the LW fill in the period gap, indicating these are likely MCVs. The periods of the LW sources are distributed more closely to those of polars (green) than the spin (black) or orbital (blue) periods of IPs.

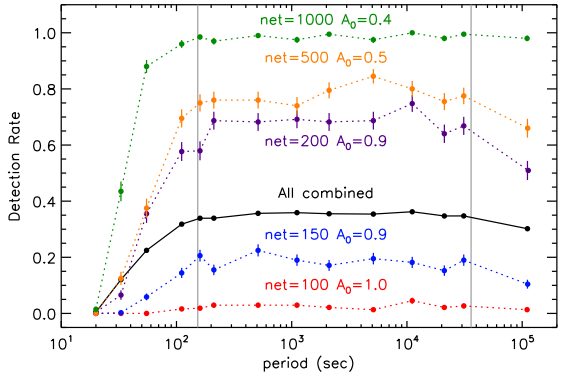


FIG. 7.— Examples of detection (P_{FAP} (Fix) < 1%) probabilities of periodicity as a function of period by simulations. The plot for "All Combined" includes the following cases: for net = 1000, A_0 = 0.2 .. 0.5, for net = 500, A_0 = 0.3 .. 0.7, for net = 200, A_0 = 0.5 .. 1.0, for net = 150, A_0 = 0.6 .. 1.0, and for net=100, A_0 = 1.0. The detection probability show no bias within the period range of the interest between 150 s to 10 hr (two vertical grey lines).

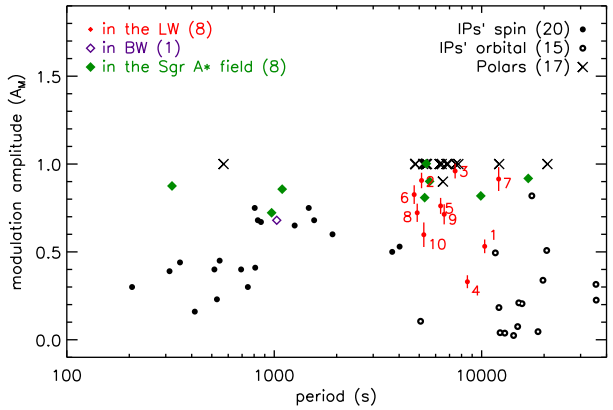


FIG. 8.— The X-ray modulation (A_M) vs. the period distribution of literature-selected IPs (black closed circles for spin periods and black open circles for orbital periods), polars (black 'x's), and the periodic sources in the LW (red circles), BW (purple diamond) and the Sgr A* field (green diamonds). [References] Orbital periods of IPs: Parker, Norton, & Mukai (2005). Spin periods of IPs: GK Per, HT Cam, EX Hya, RX J1548.2, AO Psc, V1223 Sgr, AE Aqr – Evans & Hellier (2005), V405 Aur – Evans & Hellier (2004), FO Aqu – Evans et al. (2004), PQ Gem – James et al. (2002), IGR J15094 – Butters et al. (2009), UU Col – de Martino et al. (2006), WX Pyx – Schlegel (2005), XY ARI – Salinas & Schlegel (2004), T Leo – Vrielmann et al. (2004), TV Col – Rana et al (2004), V1062 Tau – Hellier, Beardmore & Mukai (2002a), 1WGA J1958.2 – Norton et al. (2002), YY Dra – Szkody et al. (2002), V709 Cas – Norton et al. (1999). Polars: V1309 Ori – Schwarz et al. (2005), EK UMa – Beuermann et al. (2009), HU Aqr – Schwarz et al. (2009), V2301 Oph – Ramsay & Cropper (2007), SDSS J015543 – Schmidt (2005), EP Dra – Ramsay et al. (2004c), OY Car – Wheatley & West (2003), DP Leo – Ramsay et al. (2001), RX J1846.9 – Schwarz et al. (2002), V407 Vul – Marsh & Steeghs (2002), CE Gru – Ramsay & Cropper (2002), V1432 – Rana et al (2005), V347 Pav, GG Leo, EU UMa – Ramsay et al. (2004a), RX J1002-19 – Ramsay & Cropper (2002))

ally undetectable, but the spectral distinction of the plasma components between polars and IPs remains detectable in the *Chandra* X-ray band: in a quantile diagram, polars would lie in the upper-left section of $kT \sim 4-10$ keV line, and IPs in the lower-right section (Fig. 9). Although the above description of the X-ray spectra of IPs and polars is over-simplified and without a systematic survey (e.g. LWP 6 is likely a polar, see §5.6), it is generally accepted that IPs exhibit a harder spectrum. For instance, a recent survey of hard X-ray sources ($\gtrsim$ 15 keV) conducted by *Swift*/BAT and *INTEGRAL*/IBIS shows that the composition of MCVs in the hard X-ray band are predominantly IPs (Scaringi 2010).

The period range and the relative hard X-ray spectra of the LW periodic sources also resemble those of some of the periodic sources found in the Sgr A* field (green data points in Fig. 9 and blue points in Fig. 6a) (M03b). Of eight periodic sources in the Sgr A* field, four are in the same period range as the LW periodic sources with a large modulation amplitude (A_{RMS} >40% or A_M >72%), and all of them show relatively hard X-ray spectra. One of them was identified as a foreground polar, based on the light curve, and it lies at the line of kT = 10 keV and the rest lie in the $kT > 10$ keV section. In the case of the Bulge X-ray sources in the Sgr A* field, the heavy interstellar absorption ($\sim 6\times10^{22}$ cm^{-2}) may com-

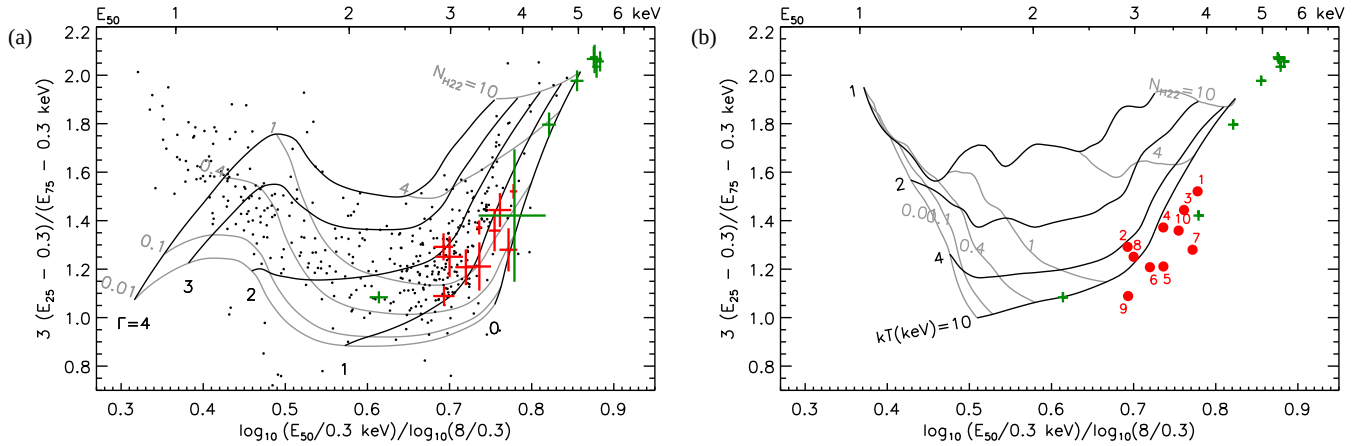


FIG. 9.— Quantile diagrams (H04, H09a) of the periodic X-ray sources in the LW (red) and the Sgr A* field (green). The same data points are plotted over a set of power model grids (a) or APEC model grids (b). The (black) dots in (a) are the discrete X-ray sources in the LW with net counts greater than 50 in the 0.3–8 keV band. The model grids are based on the response function at the aimpoint, which can be partially responsible for a small discrepancy between the spectral fit and quantile analysis in the parameter estimates for some sources (e.g. in LWP 9, $N_{\rm H22}$ = 0.2(3) from the spectral fit vs. 0.7(2) from the quantile analysis).

plicate identification of the intrinsic X-ray spectra, but for the periodic sources in the LW ($\sim 7\times10^{21}$ cm^{-2}), there is little doubt that most of them exhibit intrinsically hard X-ray spectra.

An obvious question, then, is, what is the nature of the periodic X-ray sources found in the LW and the GCR, whose period distribution resembles polars' but X-ray spectra resemble IPs'?

First, one can consider these are a rare type of polars with unusually hard X-ray spectra. Although uncertain, it is speculated that the origin of harder X-ray spectra in IPs relative to polars is related to the weaker magnetic field strength and the subsequently deeper penetration of the accretion stream into the WD surface. For instance, Cummming (2002) suggested the relatively high accretion rate in IPs effectively buries the WD magnetic field, making them appear less magnetic, which in turns helps maintaining the high accretion rate (e.g. V407 Vul: see Marsh & Steeghs 2002). This idea nicely ties the dichotomy of the magnetic field strength between IPs and polars. Under this picture, one can imagine some unusual evolutionary scenarios from IPs to polars, where polars survive with a high accretion rate that can bury the magnetic fields, allowing a harder X-ray spectrum. If most of these periodic sources are located near the Galactic center (8 kpc) as expected from the high absorption in their X-ray spectra and the high stellar density of the Bulge, the X-ray luminosities of these sources are estimated at the high end of the MCV range ($\gtrsim 10^{32}$ erg s^{-1}, see Table 3), which is also consistent with the above picture.

Second, a rare subclass of MCVs, nearly synchronous MCVs (ns-MCVs), perhaps also meet both of the observed properties - the period distribution and the relative hard X-ray spectra of the periodic sources in the LW. One can divide ns-MCVs in two subgroups - nearly-synchronous IPs (ns-IPs) and asynchronous polars (APs). Both subgroups may exhibit similar X-ray properties, but probably represent different stages in the evolutionary path of MCVs.

First, APs, consisting originally of just four systems, which recently extended to eight according to the latest RK catalog (ver 7.15), are traditionally considered as polars that are temporarily out of synchronization due to a recent Nova activity, which has altered their magnetic locking, giving $P_{\rm s}/P_{\rm o}$ ~0.98–1.02. Interestingly it is speculated that APs exhibit a harder spectrum than normal polars, but with the similar periods, as marked with purple diamonds in Fig. 6a. For instance, two of seven APs as opposed to two of 92 normal polars are found in the hard X-ray survey using *INTEGRAL*/IBIS, *Swift*/BAT and *Suzaku*/HXD (Scaringi 2010).

Second, there are increasingly more IPs found near at synchronization ($P_{\rm s}/P_{\rm o} > 0.3$). Starting with EX Hya, the list increases to six according to the RK catalog. Their orbital periods are predominantly around 1.5 hr except for V697 Sco with a 4.5 hr orbital period. According to the evolutionary model of Norton et al. (2008, hereafter N08), IPs start out with $P_{\rm s}/P_{\rm o} < 0.1$ and as the systems evolve through magnetic lock, the orbital periods decrease and the spin periods increase, i.e. $P_{\rm s}/P_{\rm o}$ approaches 1. Therefore, the orbital periods of ns-IPs will be clustered around or below the period gap near the end of the evolution, resembling the period distribution of polars more closely than that of usual, unsynchronized IPs.

As with polars exhibiting unusally hard X-ray spectra, the presence of ns-MCVs is very intriguing in terms of the evolutionary models of MCVs, challenging the conventional view of IPs with $P_{\rm s}/P_{\rm o} \lesssim 0.1$ and polars $\sim 0.98 - 1.02$. For instance, Paloma or RX J0524+42 (Pineault et al. 1987), recently identified as an AP, shows $P_{\rm s}/P_{\rm o} \sim 0.93$, and its relatively large desynchronization ($\sim 7\%$) compared to the conventional APs ($< 2\%$) suggests that this system might represent the missing link of the evolutionary path between IPs and polars (Schwarz et al. 2007), rather than polars being out of synchronization temporarily due to recent Novae activities. As shown in Fig. 6a, the gap ($\sim 0.3 - 0.95$) in the period ratio between IPs and polars are now more or less bridged by the recent discoveries of many ns-MCVs. It is speculated that some of these ns-MCVs transit between IPs and polars (e.g. V1025 Cen, see Hellier, Wynn & Buckley 2002b).

According to N08, if the period ratio exceeds 0.6, the only stable equilibrium is at synchronization ($P_{\rm s}/P_{\rm o}$ =1). Schwarz et al. (2007) suggest that the probability of finding ns-MCVs is very low, considering relatively short timescale for synchronization (< 1 Myr) compared to the lifetime of a CV ($\sim$ 100 Myr) (see also N08). Therefore, if many of the periodic sources in the LW are indeed ns-MCVs, it imposes another constraint on the evolutionary model or suggests an unusual

environment of the Galactic Bulge capable of harboring many such rare systems. The similar statement can be made for polars with unusally hard X-ray spectra.

The relative composition of source types in MCVs are highly biased, depending on search wavelengths. In the RK catalog, where most of the discoveries are based on optical/UV or longer wavelength bands, the relative ratio of IPs vs. polars are close to 1 (e.g. 83 IPs vs. 109 polars in Fig. 6), whereas a hard X-ray survey ($\gtrsim$ 15 keV) in (Scaringi 2010) revealed 37 IPs and only 2 polars (both are APs). Therefore, if many of the periodic sources in the LW are indeed unusual polars or ns-MCVs, it indicates the *Chandra* X-ray band is well tuned for discovery of these rare MCVs.

Finally we note that some of the observed X-ray properties of the periodic X-ray sources in the LW are shared by a group of quiescent Low Mass X-ray Binaries (qLMXBs). For instance, Swift J1353.5-0127, recently observed in an outburst as a black hole (BH) transient, may have a relatively short orbital period ($\sim$ 2 hr, see Casares et al. 2011) and exhibit a hard X-ray spectrum (Krimm, Kennea & Holland 2011). The observed over-abundance of X-ray transients within 1 pc of Sgr A* (cf. 4 out of 7 within 20 pc, see Muno et al. 2005) implies that a large number of qLMXBs may be present as dark stellar remnants within 1 pc of Sgr A* (Schodel et al. 2007). However, CVs (and MCVs) are expected dominantly more abundant than these BH transients, and the periodic X-ray sources in the LW do not exhibit any strong outbursts in the 1 Ms exposure spanned over 3 years (cf. out of 7 X-ray transients in the Sgr A* field, 3 or 4 sources have been observed in outbursts in each year, see Degenaar & Wijnands 2009, 2010) it is reasonable to think that the large fraction of the periodic sources in the LW are in fact MCVs.

6.2. *Periodic source content in the GCR X-ray source population*

In this section, we estimate the total number of periodic X-ray sources in the LW through completeness simulations for periodicity detection. We have generated 500 synthetic light curves for a given set of X-ray modulation parameters including modulation period and amplitude, net count and background count. Then we run the same detection algorithm to see how often the synthetic light curves are detected as periodic. This calculates $P_{\rm det}$ for the given set of parameters. Here "detection" is simply defined as $P_{\rm FAP}$ (Fix) $<1\%$[11]. The simulation is designed to match the data set observed in Epoch 4 with the same GTI gaps, and the simulated time tags are generated according to the Barycenter corrected CCD readout time cycles. The initial set of simulations indicates that the detection results do not depend on the given period range (100 s to 10 hr) (Fig. 7 in §6.1), so we fix the period at 5432.1 sec and varied the rest of the parameters. The simulated modulation amplitude (A_0) ranges from 10 to 100% in 10% increments. The simulated net counts of sources are 50, 100, 150, 200, 500, and 1000, 3000, and the background counts are 30, 50, 100, 200, 500, and 1000.

Using these simulation results, which cover most of the parameter space for the sources found in the LW, we estimate the periodicity detection probability ($P_{\rm det}$) of the 381 sources with net counts $\geq$ 100 in Epoch 4. Since we do not know a priori the distribution of modulation amplitude and the observed periodic sources show a wide range of the modulation amplitude (A_0), we randomly assign a modulation amplitude (A_0) to each source, assuming a uniform distribution from 0.1 to 1. We repeat the interpolations 10000 times (i.e. 10000 set of simulations), each with random assignments of modulation amplitude to cover the full modulation range for every source.

Fig. 10 shows an example result, using 203 sources with net counts $\geq$ 100 and $E_{50} \geq 2.5$ keV (hard X-ray sources, see also case 3 in Table 5) under the assumption that these sources are all periodic with a uniform distribution of the modulation amplitude. Fig. 10a shows the expected number of sources with detectable periodicity in the 2-D phase space of net counts vs. modulation depth for hard X-ray sources. The absolute number in each cell of the phase space depends on the cell size, so what matters here is a relative variation from cell to cell and the total number. The result shows that we expect to detect periodicity of 21(3) sources if all of the 203 sources are periodic with a uniform distribution of modulation amplitude.

Fig. 10b & c show the same result (differential and accumulated) as a function of net count. The source distribution with detectable periodicity (red) indicates that the detection probability for sources with net counts less than 150 is very low[12]. Since we only detected 9 periodic sources with $P_{\rm FAP}$ (Fix)$\leq$ 1%, this result indicates there should be about 87^{+17}_{-12} periodic sources, which is 43^{+9}_{-7}% of the 203 sources. However, since the detection probability drops significantly at net counts below 200, we cannot make a reliable assessment of the faint periodic source population. If we limit our detection probability at 1%, the dotted line in Fig. 10b shows the effective population of the sources we can explore. Accordingly the actual estimates of the periodic population can be as low as the dotted green line in Fig. 10c. Therefore, in the worst case scenario where most of the sources with net counts below 200 are not periodic, the estimated periodic source population is 50^{+10}_{-7}, which is about 24^{+5}_{-4}% of the hard X-ray sources.

Fig. 10d shows the accumulated percentage of the periodic sources in the LW as a function of net count. Fig. 10d shows a gradual increase of the fractional periodic sources as net counts decrease to 200 from 500. This observed variation of the fractional periodic sources with net counts is consistent with the fact that the X-ray fluxes of the majority of MCVs are below 10^{32-33} erg s^{-1} (Heinke et al. 2008) since the observed periodic sources are at the high end of the X-ray luminosity distribution if they are in the Bulge. It also implies the true percentage of the periodic sources with net counts less than 200 is likely higher than the value (43%) at net count $\sim$ 200.

Table 5 summarizes the simulation results that estimate the total number of periodic sources including unidentified ones among the sources found in the LW. We repeated the analysis for four sub-sets of the sources, which cover samples only with non-CCD-edge sources and hard X-ray sources ($E_{50} \geq 2.5$ keV). In this table, we show the results for sources with net counts greater than 200, where we have a sufficiently high detection probability of periodicity given the number of sources. The case using non-CCD-edge sources enables an estimate of the systematic error in our selection procedure of periodic sources since the observed periodicity of the sources that fall near a CCD edge can be falsely discredited. The case using only hard X-ray sources should be a better representative of the Bulge sources since they exclude the majority of the foreground soft sources.

[11] The result in this section is consistent with that acquired with "detection" defined as $P_{\rm FAP}$ (Var) $<1\%$.

[12] This is an over-simplification since $P_{\rm det}$ also depends on the background counts. See LWP 7 in Table 2 and §5.7.

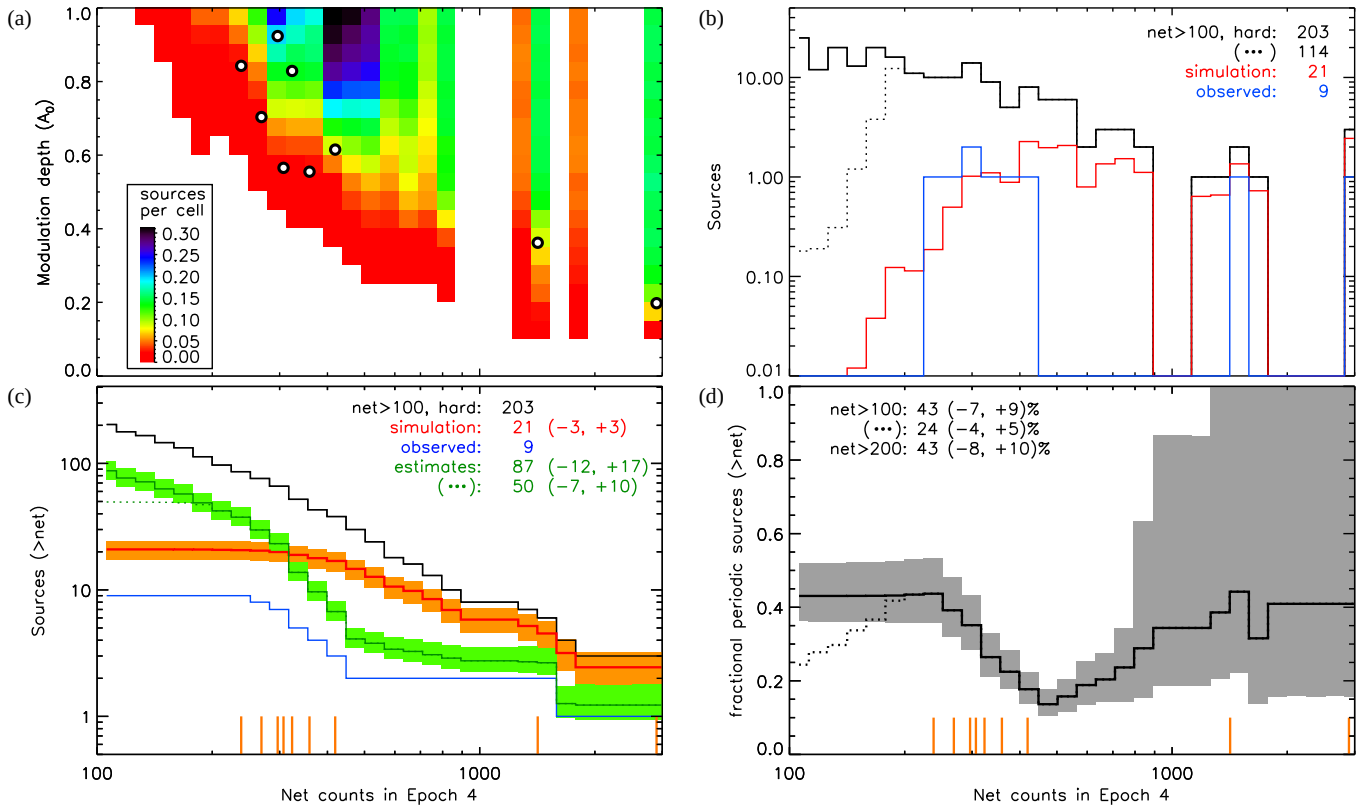


FIG. 10.— Completeness study for periodicity detection for hard X-ray sources ($E_{50} \geq 2.5$ keV; see also case 3 in Table 5). (a) The (relative) expected distribution of detectable periodic sources based on the completeness simulation under the assumption of all the sources being periodic with the uniform distribution of modulation amplitudes. The open circles show the 10 periodic sources in the LW. (b) The number of the sources with detectable periodicity (red) as a function of net count if all the sources (black) are periodic in comparison with the observed periodic sources (blue). The dotted line indicates the testable sample of the population if we limit the detection sensitivity at 1%. (c) The accumulated number of the detectable sources (red) if all the sources are periodic (black). Given the observed periodic sources (blue), we also show the expected total population of periodic sources (green). Below 200 counts, the detection sensitivity is too low to make a reliable assessment of the hidden population of periodic sources (dotted green lines). The shade for green and blue indicates the statistical errors of the simulation results and estimates. (d) The fractional percentage (solid line) of the periodic sources, which is the ratio of the green to black lines in (c). The dotted line shows a conservative limit below 200 counts due to lack of detection sensitivity, but the rapid rise of the percentage of periodic sources as the count approaches from 500 to 200 indicates the trend will continue at low counts, where the majority of the Bulge MCV populations lie (see §6.2).

TABLE 5
ESTIMATION OF THE TOTAL NUMBER OF PERIODIC SOURCES IN THE LW BY COMPLETENESS SIMULATIONS

(1)	(2)	(3)	(4)	(5)	(6)	(7)	(8)	(9)
Cases	Source Selection	Total	Periodic X-ray Sources				Alternative Estimates	
	(net $\geq$ 200 in Epoch 4)	Sources	Observed	Detectable	Estimated Total	Percentage	Estimated Total	Percentage
1	all	153(12)	9	28 (−4, +4)	48 (−6, +8)	32 (−5, +6)	48(15)	32(10)
2	non-edge	113(11)	8	21 (−4, +4)	43 (−6, +9)	38 (−7, +9)	43(14)	38(12)
3	$E_{50} \geq 2.5$ keV	96(10)	9	21 (−3, +3)	42 (−6, +8)	43 (−8, +10)	42(12)	43(13)
4	$E_{50} \geq 2.5$ keV, non-edge	69(8)	8	16 (−3, +3)	35 (−6, +8)	51 (−11, +14)	35(11)	51(16)

(1) Case number (2) Source selection criteria. We limit the sample to sources with $\geq$ 100 net counts in Epoch 4. (3) The total number of sources that meet the source selection criteria. (4) The number of the observed periodic sources from Table 2. (5) The estimated number of the detectable periodic sources by simulations under the assumption that all the sources are periodic with a uniform distribution of modulation amplitude. (6) The estimated total number of the periodic sources in source selection: (3) $\times$(4) / (5). (7) The percentage of periodic sources in the selection: (6)/(3). (8) An alternative (error) estimate of the total number of periodic sources and (9) their percentage using negative binomial distribution, where, for the observed periodic sources, N, and the non-detection probability, p, given by the simulations (in case 3, $N = 9$, $1-p = 21/100$), the estimated unidentified periodic sources and its variance are $Np/(1-p)$ and $Np/(1-p)^2$ respectively.

A simple ratio argument between the observed periodic sources and simulation results (column 6 & 7 in Table 5) indicates that about 32–38% of the sources in the LW should be, in fact, periodic and the percentage increases to 43–51% for the hard X-ray sources. The errors of these estimates are calculated from the variances of the total sample sizes (column 3) and the ranges of the detectable periodic sources (column 5), provided that at least the observed number of periodic sources (column 4) are present in each case. Alternatively one can estimate the errors for the total number of the periodic sources according to negative binomial distribution (column 8 & 9 in Table 5), which provides the variance estimates of the unidentified (and thus total) number of periodic sources.

The result indicates a large fraction of the Bulge X-ray

sources ($\gtrsim$ 30–40% of hard X-ray sources even with errors) found in the GCR should be periodic. This provides a first direct evidence for the presence of a large population of MCVs in the Bulge X-ray sources, which supports that MCVs constitute a large majority of the Bulge X-ray sources.

7. SUMMARY

We have found 10 periodic X-ray sources in the LW from the 1 MS exposure of the *Chandra* ACIS-I instrument. The overall period distribution, X-ray luminosity and spectral properties of these periodic sources and eight periodic sources found in the Sgr A* field (M03b) fit the general description of MCVs, supporting the argument that MCVs are the major constituent of the Bulge X-ray sources. However, when inspecting the details of these X-ray properties – period distribution that resembles the polars' and the hard X-ray spectra that resemble the IPs', we discover that these periodic sources may fit into rare MCVs – polars with unusally hard X-ray spectra or nearly synchronous MCVs. The completeness tests indicate at least about 40% of the hard X-ray sources in the LW are periodic, which is a first direct evidence of a large MCV population in the Bulge X-ray sources.

Given the difficulty of identifying the nature of the Bulge X-ray sources in the GCR due to high stellar density, large distance and heavy obscuration, we recommend continuous X-ray monitoring of the GCR for future discoveries of periodicity and unusual variability. Considering the importance of these unusual MCVs in understanding the evolutionary path of MCVs and their potential connection to thousands of the Bulge X-ray sources, we also encourage systematic in-depth X-ray studies of the similar kind (e.g. there are only 13 ns-MCVs with $P_s/P_o > 3$ in the RK catalog) to establish a demographic profile of their X-ray properties if any.

8. ACKNOWLEDGMENT

We thank Dr. Silas Laycock for the Magellan/IMACS observation and the initial data processing of the LW. This work is supported in part by NASA/*Chandra* grants GO6-7088X, GO7-8090X and GO8-9093X. We also thank Chandra X-ray Center (CXC) for their support in publication.

REFERENCES

Allen, K. W., 1977, Astrophysical quantities., 3rd Ed., Moskva: Mir.
Anzolin, G., 2008, A&A, 489, 1243.
Baganoff, F. K. et al. 2003, ApJ, 591, 891.
Bertin, E. & Arnouts, S., 1996, ApJ, 117, 393.
Beuermann, K. et al., 2009, A&A, 507, 385.
Bretthorst, G. L., 1988, Bayesian Spectrum Analysis and Parameter Estimation, Springer-Verlag, Berlin Heidelberg
Buccheri, R. et al. 1983, A&A, 128, 245.
Butters, C. H. et al., 2009, A&A, 498L, 17.
Casares, J. et al., 1995, MNRAS, 274, 565
Casares, J. et al., 2011, ATEL #3206
Cleveland, W. S., 1994, The Elements of Graphing Data, Hobart Press, 2nd edition.
Connors, A., 2011, in preparation.
Cumming, A., 2002, MNRAS, 333, 589
Degenaar, N. & R. Wijnands, 2009, A&A, 495, 547
Degenaar, N. & R. Wijnands, 2010, A&A, 524, 69
de Martino, D. et al., 2006, A&A, 454, 287
Dolphin, A. E., 2000, PASP, 112, 1383.
Drimmel, R., Cabrera-Lavers, A., & Lopez-Corredoira, M., 2003, ApJ, 409, 205.
Evans, P. A. & Hellier, C., 2004, MNRAS, 353, 447.
Evans, P. A. et al., 2004, MNRAS, 349, 715.
Evans, P. A. & Hellier, C., 2005, ASP conference Series, 303, 2005.
Evans, P. A. & Hellier, C., 2007, ApJ, 663, 1277.
Freeman, P.E. et al. 2002, ApJS, 138, 185.
Gehrels, N. et al. 1986, ApJ, 303, 336.
Grindlay, J.E. et al., 2005, ApJ, 635, 907.
Grindlay, J.E. et al., 2011, in preparation.
Heinke, C. O., et al., 2008, AIPC, 1010, 136.
Hellier, C., Beardmore, A. P., Mukai, K., 2002, A&A, 389, 904.
Hellier, C., Wynn, G. A., Buckley, D. A. H., 2002, MNRAS, 333, 84.
Hong, J, Schlegel, E. M. & Grindlay, J. E., 2004, ApJ, 614, 508. (H04)
Hong, J. et al. 2005, ApJ, 635, 907 (H05).
Hong, J. et al. 2009a, ApJ, 699, 1053 (H09a).
Hong, J. et al. 2009b, ApJ, 706, 223 (H09b).
Hong, J, et al. 2011, in preparation.
James, C. H. et al., 2002, MNRAS, 336, 550.
Koenig, X. et al. 2008, ApJ, 685, 463.
Krimm, H., Kennea, J. A. & Holland S. T., 2011, ATEL #3142
Laycock, S. et al. 2005, ApJL, 634, 53 (L05).
Leahy, D. A. et al. 1983, ApJ, 266, 160
Marsh, T. R. & Steeghs, D., 2002 MNRAS, 331L, 7
Marshall, D. J. et al. 2006, A&A, 453, 635
Muno, M. P. et al. 2003a, ApJ, 589, 225 (M03a)
Muno, M. P. et al. 2003b, ApJ, 599, 465 (M03b).
Muno, M. P. et al. 2004, ApJ, 613, 1179 (M04)
Muno, M. P. et al. 2005, ApJL, 622, 113
Muno, M. P. et al. 2009, ApJS, 181, 110 (M09)
Norton, A. J. et al., 1999, A&A, 347, 203
Norton, A. J. et al., 2002, A&A, 384, 195
Norton, A. J., Wynn, G. A. & Somerscales, R. V., 2004 ApJ, 614, 349
Norton, A. J., et al., 2008 ApJ, 672, 524
Parker, T. J., Norton, A. J., & Mukai, K., 2005, A&A 439, 213
Patterson, J., 1998, PASJ, 110, 1132.
Pineault, S., Landecker, T. L., & Routledge, D., 1987, ApJ, 315, 580
Predehl, P. & Schmitt, J. H. M. M., 1995, A&A, 293, 889.
Protassov, R., et al., 2002, ApJ, 571, 545.
Ramsay, G. et al. 2001, MNRAS, 326L, 27.
Ramsay, M. & Cropper, M. 2002, MNRAS, 335, 918.
Ramsay, M. & Cropper, M. 2003, MNRAS, 338, 219.
Ramsay, G. et al. 2004a, MNRAS, 347, 95.
Ramsay, G. et al. 2004b, MNRAS, 350, 1373.
Ramsay, G. et al. 2004c, MNRAS, 354, 773.
Ramsay, M. & Cropper, M. 2004, MNRAS, 347, 497.
Ramsay, M. & Cropper, M. 2007, MNRAS, 379, 1209.
Ramsay, G. et al. 2008, MNRAS, 387, 1157.
Rana, V. R. et al., 2004, AJ, 127, 489.
Rana, V. R. et al., 2005, ApJ, 625, 351.
Revnivtsev, M., et al., 2009 Nature, 458, 1142.
Revnivtsev, M., et al., 2010 A&A, 515, 49.
Revnivtsev, M., et al., 2011, astro-ph/1101.5883
Ritter, H. & Kolb, U., 2003, ApJ, 404, 301
Ruiter, A., Belczynski, K. & Harrison, T. 2006, ApJL, 640, 167.
Salinas, A. & Schlegel, E. M., 2004, AJ, 128, 1331
Scargle, J. D., 1982, ApJ, 263, 835.
Scargle, J. D., 1982, ApJ, 504, 405.
Scaringi, S., et al., 2010, MNRAS, 401, 2207.
Schlegel, D., Finkbeiner, D. & Davis, M., 1998, ApJ, 500, 525.
Schlegel, E. M., 2005, A&A, 433, 635
Schmidt, G. D., 2005, ApJ, 620, 422
Schodel, R. et al., 2007, A&A, 469, 125
Schwarz, R., et al., 2002, A&A 392, 505.
Schwarz, A. D., et al., 2007, A&A 473, 511.
Schwarz, R., et al., 2005, A&A 442, 271.
Schwarz, R., et al., 2009, A&A 496, 833.
Szkody, P. et al., 2002, AJ, 123, 413.
Sumi, T., 2004, MNRAS, 349, 193.
Udalski, T., 2002, ACTA Astronomica, 52, 217.
van den Berg, M. et al.. 2006, ApJL, 135, 647.
van den Berg, M. et al. 2009, ApJ, 700, 1702. (B09)
Vrielmann, S., Ness, J.-U., Schmitt, J. H. M. M., 2004, 4A&A, 419, 673V.
Wang, Q. D. , Gotthelf, E. V. & Lang, C. C., 2002, Nature, 415, 148.
Warner, B., 1995, Cataclysmic Variable Stars, Cambridge Univ. Press, New York
Wheatley, P. J. & West, R. G., 2003, MNRAS, 345, 1009.
Zhao, P. et al. 2005, ApJS, 161, 429.